Garnet fracturing reveals ancient unstable slip events hosted in plate interface metasediments

Samuel Angiboust, Paraskevi Io Ioannidi, Iskander Muldashev

Earth Planet. Sci. Lett. 640 (2024) 118794

Contents lists available at ScienceDirect

Earth and Planetary Science Letters

journal homepage: www.elsevier.com/locate/epsl

Garnet fracturing reveals ancient unstable slip events hosted in plate interface metasediments

Samuel Angiboust [a,b,*], Paraskevi Io Ioannidi [c], Iskander Muldashev [d,e]

[a] ENS de Lyon, LGL-TPE, CNRS, 46 Allée d'Italie, Lyon, France
[b] Institut Universitaire de France (IUF), France
[c] Department of Earth Sciences, Vrije Universiteit Amsterdam, Amsterdam, the Netherlands
[d] GFZ German Research Centre for Geosciences, Potsdam, Germany
[e] TU Bergakademie Freiberg, Freiberg, Germany

ARTICLE INFO

Editor: Carolina Lithgow-Bertelloni

Keywords:
Numerical modelling
Garnet
Fracturing
Metasediment
Paleoseismicity

ABSTRACT

A paradox exists between the great number of intermediate-depth earthquakes occurring along active subduction interfaces worldwide and the extreme scarcity of paleo-seismic events recorded in exhumed metasediments from ancient subducted slabs. Recrystallization associated with exhumation-related overprinting generally contributes to the nearly-complete erasing of markers of unstable slip events in metamorphic rocks. We herein focus on a sample from an ancient deep thrust from a Cretaceous High-Pressure paleo-accretionary complex in Chilean Patagonia. A representative, moderately foliated micaschist exhibits broken garnet crystals that host a dense network of healed micro-fractures. While garnet fragments appear thoroughly disaggregated along the main foliation, the rock matrix that completely recrystallized has lost the record of brittle deformation. We employ a 2D visco-elasto-plastic numerical modelling approach in order to investigate the mechanical conditions that enable the fracturing of isolated garnet grains in a relatively weak matrix. The rupture of these stiff grains is achieved in our models at strain rates faster than 10^{-10} /s to 10^{-12} /s for elevated pore fluid pressures (80 to 99 % of the lithostatic value, respectively). Since high pore fluid pressures prevail in deep subduction interface settings, it is suggested that the rupture of these garnet crystals occurred through cataclastic deformation via (transient) slip rate acceleration, perhaps as a consequence of localized slip associated with slow to conventional earthquakes. Upon slip rate deceleration, viscous disaggregation of the broken garnet clasts occurred along with the erasing of the matrix cataclastic fabric.

1. Introduction

Thousands of earthquakes occur every year at the base of the seismogenic zone along the 'upper seismic plane' in active subduction margins worldwide at conditions where the downgoing crust experiences metamorphic recrystallization under blueschist to eclogite-facies conditions (most commonly between 35 and 70 km depth and 300–600 °C depending on the geothermal gradient; Hacker et al., 2003). Geodetic data has also demonstrated that this region of the plate interface hosts abundant slow earthquakes and post-seismic slip of megathrust ruptures (e.g. Alaska: Freymueller et al., 2008; Chile: Lange et al., 2012; Luo and Wang, 2021). The physical nature of the processes that cause the upper-plane seismicity remains a matter of debate (e.g. Shiina et al., 2013; Incel et al., 2017). High-resolution seismological studies confirm that the bulk of this upper plane seismicity is hosted in the downgoing crust (e.g. Sippl et al., 2018) even though the resolution does not enable distinguishing whether these earthquakes nucleate in metasediments or in the underlying mafic crust.

Exhumed metamorphic rocks represent precious witnesses of deformation processes taking place at depth along the subduction interface (e.g. Bebout and Penniston-Dorland, 2016; Behr and Bürgmann, 2021). On the one hand, recent field and structural investigations have emphasized the prevalence of pressure-solution processes during creep in both hydrothermalized metabasalts and metasediments which together contribute to maintaining the plate interface strength at relatively low stress levels on geological timescales (e.g. Wassmann and Stöckhert, 2013a; Tulley et al., 2020; Condit et al., 2022). On the other hand, the scarce evidence for paleoseismicity in exhumed subduction zone

* Corresponding author.
E-mail address: samuel.angiboust@ens-lyon.fr (S. Angiboust).

https://doi.org/10.1016/j.epsl.2024.118794
Received 28 February 2024; Accepted 19 May 2024
Available online 29 May 2024

high-pressure (HP) metamorphic rocks appears to be restricted to relatively stiff lithologies like metagabbros in the form of fault-zone rocks such as 'pseudotachylytes' (John and Schenk, 2006; Austrheim and Andersen, 2004) or 'eclogite breccias' (Angiboust et al., 2012) as well as within 'foliated cataclasites' in blueschist-facies metabasalts (Muñoz-Montecinos et al., 2021).

To our knowledge, no evidence for fast-slip brittle structures (i.e. structures on which slip occurred at the order of millimeters to meters per second) has been identified in deep-seated ($T > 450°$) metasedimentary rocks from ancient subduction interface settings. This observation can easily be explained by (i) the relatively weak nature of quartz, carbonate and mica-bearing lithologies that dominantly compose the matrix of HP metasedimentary rocks (e.g. Smye and England, 2023 and references therein) (ii) the long residence time of accreted metasediments in deep duplex structures forming above the plate interface that enable petrological re-equilibration and the destruction of previously-formed brittle fabrics (e.g. Sibson, 1980; Kirkpatrick and Rowe, 2013) and (iii) the high pore fluid pressures that also catalyze re-equilibration and recrystallization processes along grain boundaries.

This paradox calls for a re-investigation of microstructures in exhumed HP metasediments, in particular within 'strong' minerals which may have greater chances to preserve remnants of 'lost' unstable slip events in their inner structure. We herein focus on the aspect, the size distribution and the chemical zoning patterns of broken garnet crystals in a banded micaschist sample from the Cretaceous Patagonian HP paleo-accretionary belt. Because stiff, isolated crystals such as garnet are expected to rotate –instead of breaking– during the shearing of a rheologically weak metasedimentary matrix (e.g. Passchier et al., 1992), we perform numerical modelling investigations in order to identify the physical parameters that can allow the fracturing of a strong particle in a relatively low viscosity environment.

2. Geological setting

The Diego de Almagro island represents one of the very rare exposures of the Mesozoic Chilean paleo-accretionary complex (Hervé and Fanning, 2003) and the first occurrence of eclogite-facies metamorphism in Chile (Hyppolito et al., 2016). The three main units exposed on this island have been formed by episodic basal accretion of material derived from the Pacific oceanic plate during Jurassic to Cretaceous times (Fig. 1a; Angiboust et al., 2018). The studied sample (#47a) has been collected in the uppermost part of the 'garnet amphibolite' unit in the footwall of the Puerto Shear Zone, a major tectonic contact interpreted as constituting the ancient subduction interface hanging wall after accretion of the overlying Lazaro unit during the middle Jurassic (Fig. 1b; Angiboust et al., 2018). Petrological investigations, thermodynamic modeling and ion probe U-Pb zircon rim dating have shown that peak burial conditions were reached at around 130 Ma, for a pressure (P) of c.1.7 GPa and a temperature (T) of 550–570 °C (Hyppolito et al., 2016; Angiboust et al., 2018). The garnet amphibolite unit (in green in Fig. 1b) has been re-equilibrated upon exhumation along the subduction interface at 1.3 GPa (approximately 45 km depth; Fig. 1c), where it underwent fracturing and shearing associated with moderate amphibolitization (Hyppolito et al., 2016). Then, it has been juxtaposed to the existing duplex and was later exhumed (and partly overprinted in the greenschist facies) via long-lived underplating processes throughout the entire fore-arc crust (e.g. Angiboust et al., 2022).

3. Petrographic observations

3.1. Petrography and structure of the studied sample

The matrix of the sample #47a (made in the XZ plane of the sample)

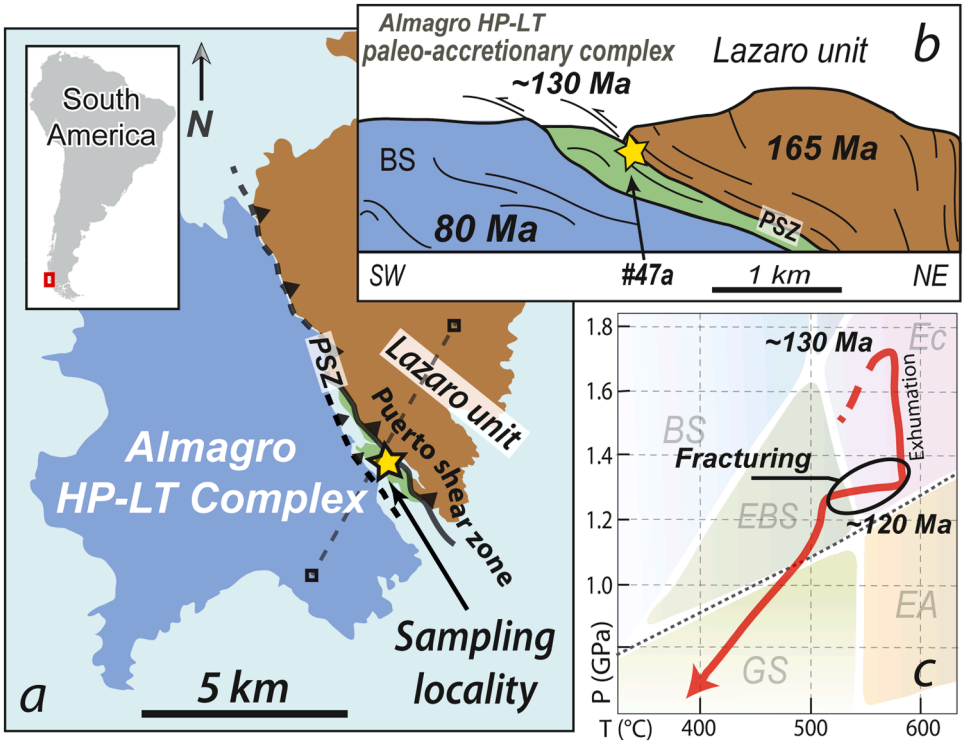

Fig. 1. Geological context of the studied sample. a and b. Simplified geological map and cross-section showing the structure of the island comprising three main tectonic slivers with peak pressure deformation ages of 165 Ma (Lazaro unit: brown), 130 Ma (Garnet amphibolite unit: green, from which the studied sample #47a indicated by yellow star comes from) and 80 Ma (Blueschist unit: BS: blue). PSZ: Puerto Shear Zone. GPS coordinates of sample #47a: *S 51° 34′ 52″, W 75° 11′ 59″*. c. Pressure-Temperature path followed by the studied sample (#47a) during Cretaceous burial-exhumation history (Hyppolito et al., 2016). The studied fracturing event occurred at near 120 Ma, 550 °C and 1.3 GPa (approximately 45 km depth).

is heterogeneous at the cm-scale with interbedded pale bands of quartzitic micaschists and deep blue-green, mafic metatuffaceous discrete layers (Fig. 2a,b,c; Fig.S3). The matrix of pale bands is mostly made of quartz (~40 vol. %) and white mica (phengite, 20–30 %) that hosts discrete amphibole crystals (less than 10 %), garnet crystals (less than 5 %), and post-kinematic albite porphyroblasts (~10 %). Other minor phases comprise rutile (rimmed by titanite), chlorite and epidote which all together make less than 5 % of the rock volume (volumes based on visual estimation charts; Fig. 2b). The matrix of mafic bands hosts abundant amphibole crystals (30–35 vol. %) interleaved with phengite laths (~13 %), chlorite (5 %) and interstitial quartz (15 %; Fig. 2c). Garnet porphyroclasts represent 15–20 vol. % of the dark band volume. Albite (c.10 vol. %) occurs within garnet pressure shadows as well as discrete individual, 100–500μm-wide porphyroblasts in the matrix. Other minor phases comprise interstitial diopside (3 %), epidote (3 %) and rutile-titanite aggregates (1 %). Rare crystals of omphacite, glaucophane and chloritoid, remnants from the eclogite-facies stage, are locally preserved as inclusions in garnet mantles from the mafic parts (Hyppolito et al., 2016). The moderately strained matrix has recrystallized during an upper amphibolite-facies shearing event associated with exhumation at c.120 Ma (multi-mineral Rb-Sr dating; Hyppolito et al., 2016, 2019; Fig. 1c). This event led to the partial re-equilibration of peak pressure garnet (garnet I) along its rims (garnet II). These two garnet generations, optically distinguishable on Fig. 3d, can be identified on back-scattered electron mode at the scanning electron microscope both in the pale micaschist and the dark mafic band (SEM; Fig. 3c; see Appendix for analytical conditions and for additional textural images). Automated surface estimations indicate that garnet I represents 10 surf. % and garnet II 2 surf. % of the area mapped in Fig. 3c (which represent a part of the mafic band shown in Fig. 2c). Garnet internal structure exhibits a general increase of its XMg content towards the rims (Fig. 3a).

Numerous chemical oscillations, well-marked on the Mn map (Fig. 3b), are transected by several overgrowths (white arrow) and crosscut by numerous healed micro-fractures observed within both garnet generations (Fig. 3e,f,g). These micro-fractures are well expressed on the XMg map and connect the matrix with the garnet interior. Angular, broken garnet I clasts are commonly rimmed by a euhedral, facetted garnet II generation, that may or may not exhibit fracturing (Fig. 3e,f,g; see also Fig.S1 and S2). Most large garnet crystals display healed fractures cutting straight across the crystal nearly linearly (Fig. 3c; Fig. S1). In addition to micro-fracturing, some of the garnet zoning patterns display indentation features (see white arrows on Fig. 3e,f,g) and subsequent enhanced garnet facet dissolution (e.g. Wassmann and Stöckhert, 2013b). No clear evidence for subcritical crack growth (in the sense of Atkinson, 1984) has been detected using BSE or X-ray imaging. Garnet clast diameter typically ranges from several tens of microns to c.4 mm. Most of the garnet I clasts exhibit a surface smaller than 0.05 mm^2 (Fig.S4).

The matrix around garnet crystals exhibits only very discrete evidence for fracturing: microstructural evidence of fracturing has been only detected in the core of some albite porphyroblasts using optical cathodoluminescence imaging (see Fig.S3). None of the other phases forming the studied sample (amphibole, diopside) exhibits evidence for micro-fracturing, which seems to be mostly recorded within garnet. The vast majority of the crystals forming the matrix exhibit a moderate shape-preferred orientation (especially white micas) along with indication of crystal-plastic deformation (well visible in quartz) as well as extensive evidence for pressure solution creep processes (PSC; see also Muñoz-Montecinos et al., 2020 for similar observations in Chilean basement rocks). Last, we note that similar (but less well-visible) fracturing patterns were observed in garnet from other samples from the same unit (the garnet amphibolite unit, Fig. 1b; see also Fig.S2), indicating the pervasiveness nature of the studied fracturing process along the Puerto Shear Zone.

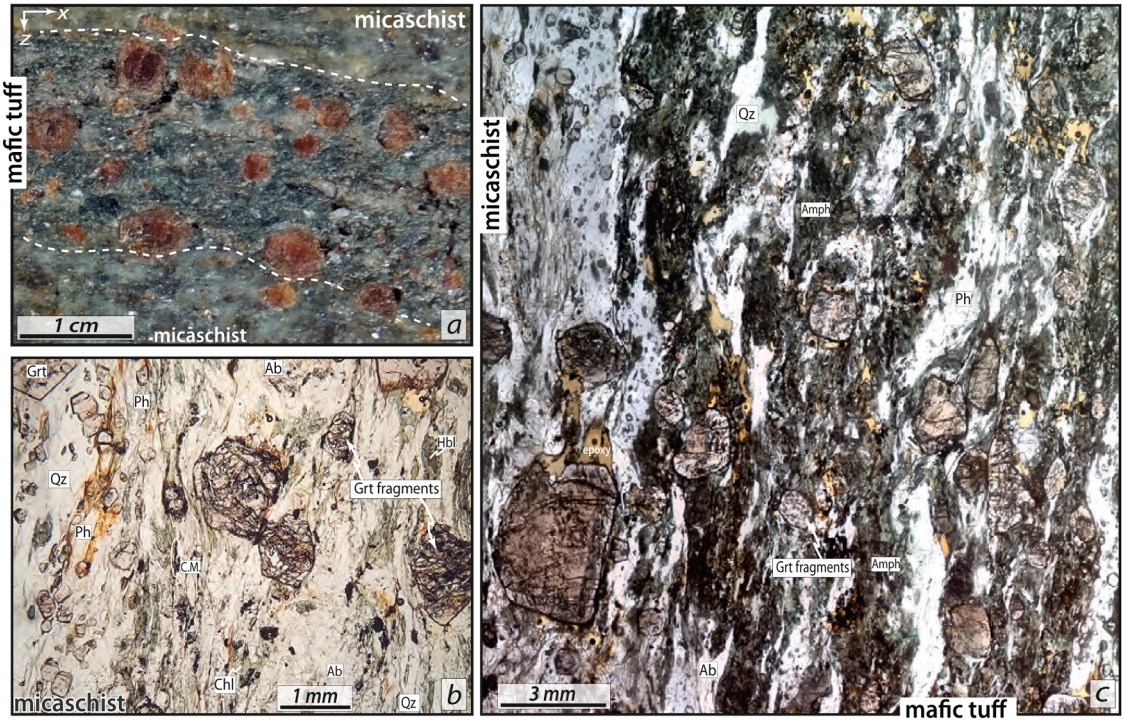

Fig. 2. Petrographic description. a. Hand specimen photograph of the studied sample showing 1–3 mm sized garnet porphyroblasts in a foliated matrix comprising albite, phengite, amphibole, epidote and quartz. b. Optical microscope picture (plane polarized light, x2.5) showing a representative area of the pale (leucocratic) micaceous region of the sample. Abbreviations after Whitney and Evans (2010); C.M.: carbonaceous matter. c. Scan of the studied thin section showing the quartzitic micaschist region (left) and the mafic tuffaceous band (right).

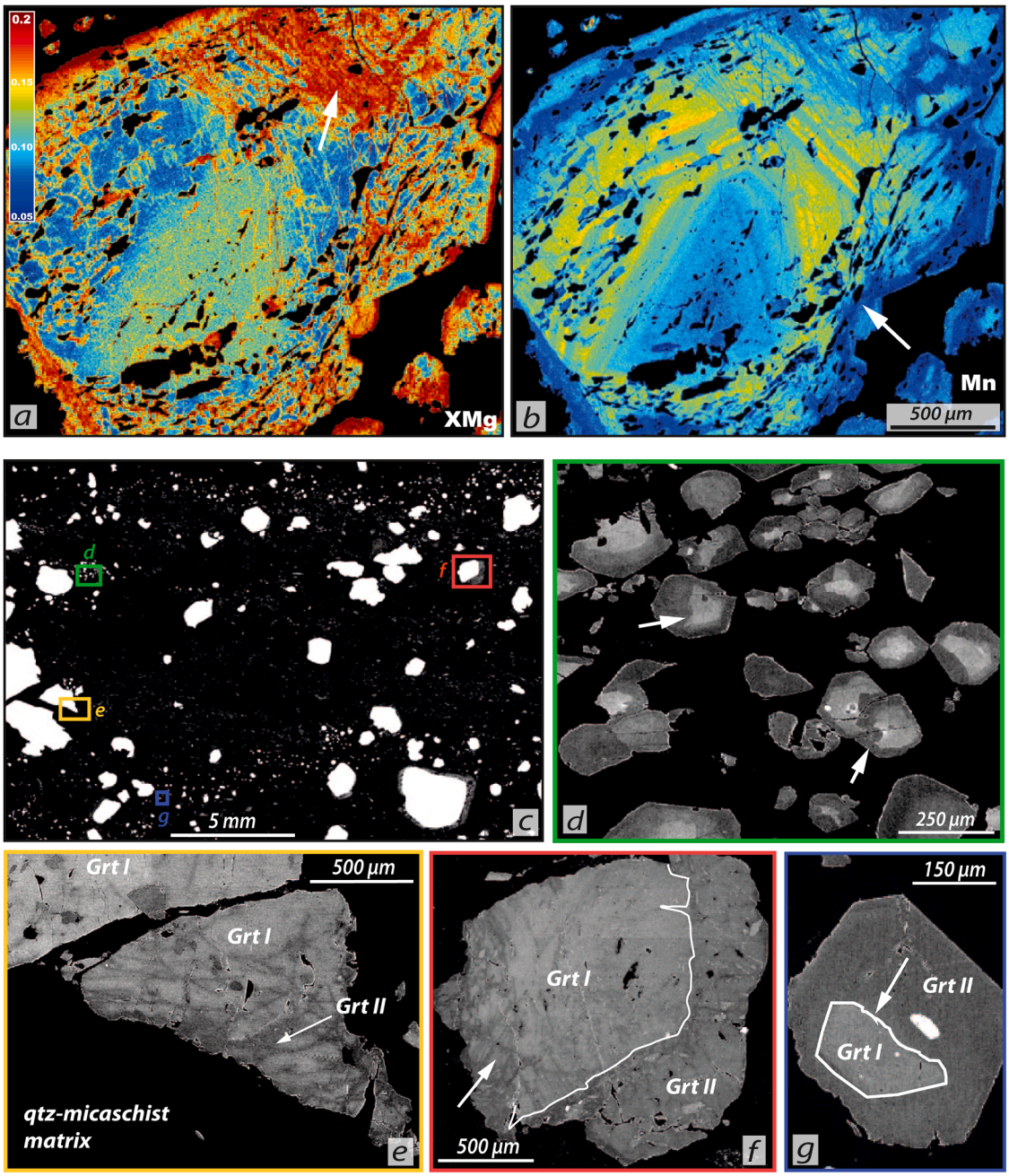

Fig. 3. Petrographic description. a and b X-ray maps showing the internal XMg (Mg/Mg+Fe) and Mn zoning structure of a large garnet crystal from sample #47a. Note the remarkable density of healed fractures as well as the dissolution of the garnet right side marked with a white arrow on panel d. c. EDS mapping of a part of the studied thin section showing the distribution of garnet grains (Grt I cores have been colored in white for better visibility). d to g. BSE pictures showing the internal zoning structure of garnet grains from the studied sample (see Fig. 2c for garnet clast emplacement). The observation of darker, healed garnet fractures even in the second garnet generation (see Fig. 3f) indicates that several fracturing events occurred during and after the formation of Grt II.

3.2. Mineralogical evolution of the sample

Because of the protracted nature of the sequence of metamorphic events (at least three) that affected this sample, the observed amount of phases visible in the present sample should not be considered as a direct representation of the volumetric proportion of phases that were present during amphibolitization, i.e. when the studied fracturing event occurred. This is particularly true for albite and chlorite that both mostly grew during the greenschist overprint that affected the entire unit when crossing the greenschist facies field (Fig. 1c). In order to evaluate the nature of phases present during amphibolitization in both micaschist and mafic tuff bands, we use a thermodynamic modelling approach with the software package Perplex (Connolly, 2005) following the same calculation procedure, models and bulk compositions as in Hyppolito et al. (2016; see details on the modelling approach and results in Table S1). Note that because of the strong thermodynamic disequilibrium that exists during exhumation of this sample, the mineral proportions estimated for the amphibolitization stage should not be directly transposed to the mechanical models below. Taking into account this important consideration, we can estimate that, depending on local bulk chemistry, between 10 and 20 % of garnet crystals were present in the mafic bands during fracturing in the amphibolite facies (Fig. 2c). This proportion drops to less than 5 % for the pale quartz-rich micaschist domains (Fig. 2b). Combining modelling and petrographic observations,

we can estimate that albite was rare to nearly absent during the fracturing event at 1.3 GPa (from 0 to less than 5 %). Quartz and mica proportions remained roughly constant upon exhumation as predicted by the thermodynamic models.

4. Numerical modeling

4.1. Modeling approach

In order to model simple shear of a matrix with garnet inclusions we use the thermomechanical Finite Element Method (FEM) code SLIM3D (Popov and Sobolev, 2008), which solves the conservation equations of mass, momentum, and energy. The code uses a marker-in-cell method and employs a visco-elasto-plastic deformation pattern. The finite elements are isometric with a size of 0.1 mm while the 2D model domain is 105 mm wide and 50 mm deep (Fig. 4). We run two sets of models which differ only in their matrix rheologies (quartzitic and amphibolitic) to account for the two distinct layers found in our studied sample (see above). The garnet crystals of fixed size (diameter equals 5 mm) are distributed randomly covering 10 % of the model area, for both sets of models. This value represents an average between the amount of garnet estimated for the more quartzitic bands and the more mafic layers. Recent numerical models have demonstrated that increasing the amount of rigid bodies from 10 to 20 or 25 % does not notably change the bulk rheology of the mixture (Ioannidi et al., 2021).

To create homogeneous distribution and prevent boundary effects (and in the absence of information of garnet distribution at the time of fracturing in the amphibolite facies), garnet crystals are distributed with the rule that none of them can be positioned at the distance smaller than the garnet diameter from other garnet or model boundary.

We use temperature of 550 °C and lithostatic pressure of 1.3 GPa, in order to match the inferred conditions of brittle deformation in the studied Patagonian sample. Hence, we assume that dislocation creep, $\dot{\varepsilon}_{dis}$, is the only mechanism of viscous deformation, $\dot{\varepsilon}_{visc}$, in the model:

$$\dot{\varepsilon}_{visc} = \dot{\varepsilon}_{dis} = A\tau_{II}^{n} exp\left(\frac{-Q}{RT}\right) \quad (1)$$

where A, n and Q are dislocation creep constants, R is the universal gas constant, τ_{II} is the square root of the second invariant of the deviatoric stress tensor, and T is the temperature.

We use the Drucker-Prager criterion for plasticity:

$$\tau_y = C \cdot cos\alpha + P \cdot (1-\lambda) \cdot sin\alpha \quad (2)$$

$$P = P_{lith} + P_{dyn} \quad (3)$$

$$\lambda = \frac{P_f}{P_{lith}} \quad (4)$$

where τ_y is the yield strength, C is the cohesion, μ is the coefficient of friction (30° for both phases), P is the total pressure, λ is the pore fluid pressure ratio, P_{lith} is the lithostatic pressure, P_{dyn} is the dynamic pressure, and P_f is the pore pressure. All rheological properties of matrix and garnet are described in Table 1. In order to evaluate the effect of matrix viscosity and to reproduce the sample lithological heterogeneity, we used two distinct flow laws: one for quartz from Gleason and Tullis

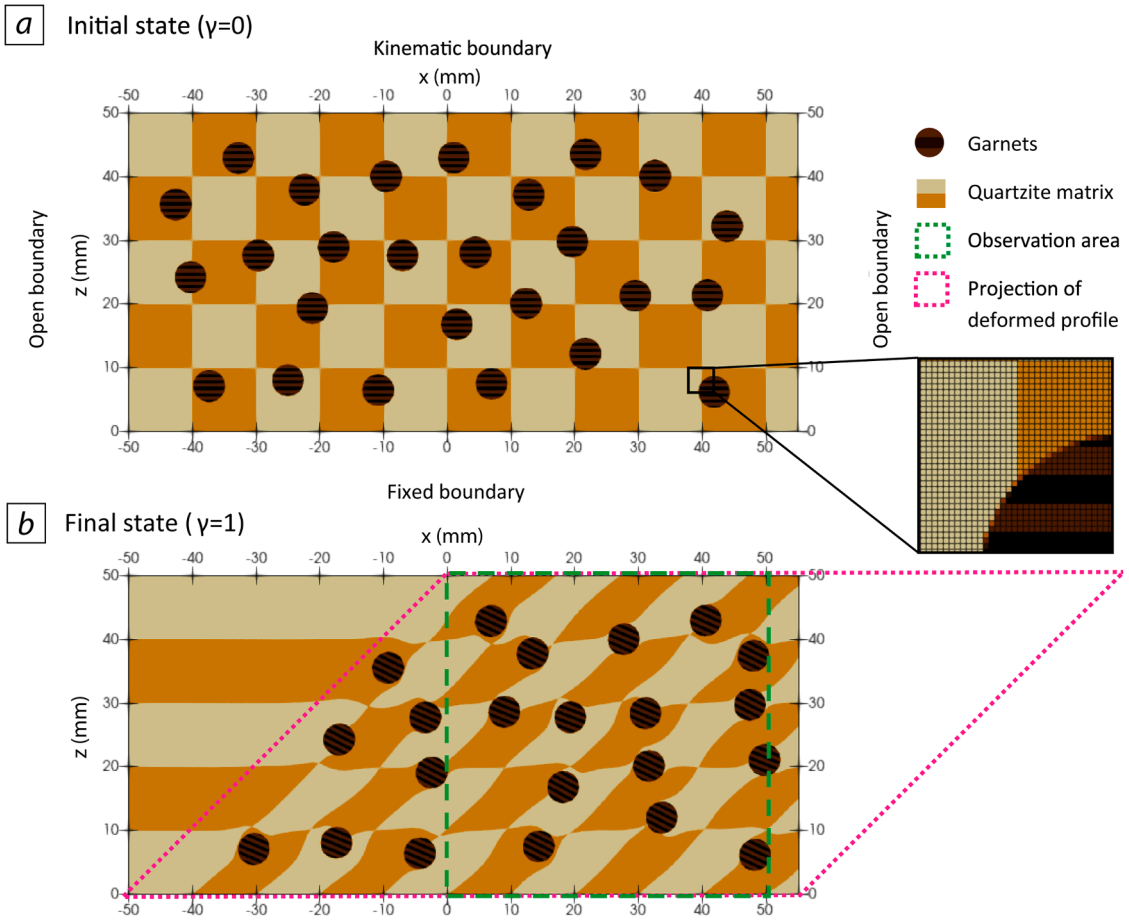

Fig. 4. Modelling – methodology. a. Snapshot of material distribution at initial state with zoomed in area showing elements' mesh, where orange-beige checkerboard background denotes quartzite matrix and brown circles with black stripes denote garnets. b. Snapshot of the material distribution at the final state after achieving shear strain (γ) value of 1. Magenta dotted frame denotes projection of deformed profile and green dashed line denotes observation area with the size of 50 mm.

Table 1
Rheological parameters for the materials used in the numerical models. Flow parameters for garnet are from Ji and Martignole (1994), from Gleason and Tullis (1995) for quartz (matrix) and from Hacker and Christie (1990) for the amphibolite matrix.

	Quartzite micaschist matrix	Amphibolitic matrix	Garnet
Density (kg/m^3)	2800	2800	3700
Shear modulus (GPa)	40.0	40.0	94.0
Bulk modulus (GPa)	63.0	63.0	171.0
Cohesion (MPa)	50.0	50.0	50.0
Friction angle	30	30	30
Log(A) factor (1/Pa^n/s)	−28.0	−26.2	−6.55
Activation energy (kJ/mol)	223	244	485
Exponent	4.0	3.7	2.22

(1995) for the quartzitic micaschist and one designed for an amphibolite from Hacker and Christie (1990) for the mafic metatuffaceous band. Because garnet plasticity is not detected in our sample, the relatively strong garnet flow law from Ji and Martignole (2004) has been chosen to model the rigid bodies.

4.2. Model setup

We use a fixed boundary at the bottom, open boundaries at the sides, and kinematic boundary with horizontal velocity, v, at the top. Velocity, v, at the top is chosen to reproduce particular bulk shear strain rate $\dot{\gamma}$:

$$v = \dot{\gamma} \cdot h \tag{5}$$

where h is the model's depth (50 mm).

As garnet crystals move to the right direction during the run of the model, we do not add new garnet crystals. The final state of the model is achieved after bulk shear strain γ reaches a value of 1, i.e., a displacement of the top boundary by 50 mm. At the final state, the model includes empty space in the form of a triangle at the left side of the model. In this way, we observe deformations of the model only in the right half of the model (the range of x axis from 0 to 50 mm) which is framed with a green dashed line in Fig. 4b.

4.3. Styles of deformation

In this study, we explore the parameter space of the bulk shear strain rate, $\dot{\gamma}$, and pore fluid pressure ratio, λ. We vary the bulk shear strain rate, $\dot{\gamma}$, in the range between 10^{-15} and 10^{-4} 1/s which are representative of typical deep subduction interface strain rates (e.g. Oncken et al., 2022 and references therein). Although it is widely accepted that the pore fluid pressure ratio, λ, in subduction interface varies in the range 0.9 – 0.99 (Sobolev and Babeyko, 2005; Lamb, 2006; Moreno et al., 2014; Angiboust et al., 2015), we vary λ from 0.37 (hydrostatic pressure) to 0.995 to cover all possible cases.

We classify models by their stress state; for this, we introduce the parameter of normalized stress σ_{norm}, which is equal to the ratio of the average shear stress on the top of the model (approximated by the square root of the second invariant of the deviatoric stress tensor, τ_{II}) and the theoretical yield strength of the material (Eq. (2)):

$$\sigma_{norm} = \frac{\tau_{II}}{\tau_y} \tag{6}$$

Note that this parameter cannot be higher than 1. In this way, along with observations of the style of deformation in the model, we track the evolution of the normalized stress over the shear strain (Fig. 5a).

Since garnet crystals cannot cross the kinematic boundary of the model, the average shear stress on the top of the model mostly characterizes the state of the matrix. In the beginning of the simulation, when there is no elastic stress in the model, shearing results in elastic loading of the model. Later, stress reaches peak value and remains relatively constant (Fig. 5a). The peak value depends on the style of deformation inside the model. We distinguish 4 styles of deformation (Fig. 5b). For the sake of clarity and simplicity, in Fig. 5 we only show models with λ = 0.75 and bulk shear strain rate, $\dot{\gamma}$, of 10^{-12}, 10^{-10}, 10^{-9}, and $10^{-7.5}$ 1/s, which however cover the whole range of deformation styles observed in the models. Note that all these (and the following) mechanical properties are shared between the garnet-quartzite and the garnet-amphibolite models. However, for the sake of clarity, we focus on the results of the garnet-quartzite models.

The first style is characterized by the absence of any frictional deformation (Style 1 in Fig. 5b). While the matrix deforms in a viscous way, garnet crystals remain undeformed. However, shearing of the model results in rotation of the garnet crystals. Notably, the highest strain rate is observed in the vicinity of garnet crystals, especially those closer to other garnets (in line with earlier observations by Kenkmann and Dresen (1998), and more recent results by Vrijmoed and Podladchikov (2015). Since there is no frictional deformation, peak shear stress on the top surface is below yield strength (Eq. (2)) and regulated by the viscous parameters of matrix, temperature and bulk shear strain rate. Also, as the matrix deforms viscously, the stresses in the matrix are lower than in the garnets which remain elastically loaded and do not relax the stresses viscously. In this way, friction of the matrix and garnet crystals as well as pore fluid pressure have no effect on stress in the model.

The second style (Style 2 in Fig. 5b) is similar to the first one, with the difference that frictional deformation appears on the rims of garnet crystals. Nevertheless, even though frictional deformation is present, we cannot exclude that its occurrence is a numerical artifact, and in this case, the second style would become the same as the first one. Since in our models we use regular quadratic mesh, elements on the borders of circular garnets contain markers of both materials (inset of Fig. 4a). Existence of both types of markers in one element results in the averaging of rheological properties of that element and leads to localization of stresses and subsequently frictional deformation (e.g., Ioannidi et al., 2022). Shear stress inside of garnet crystals is higher than in matrix as in style 1, however, stress on the rims of garnet crystals reaches yield stress (note for the model with λ = 0.75, yield stress τ_y=205.8 MPa according to Eq. (2)).

In the models of the third style (Style 3 in Fig. 5b) frictional deformation occurs inside the garnet crystals, while the matrix remains viscous. In these models, garnet crystals both deform frictionally and rotate. The peak value of the stress on the top surface stays below yield strength due to the ability of the matrix to release stress load in the form of viscous deformation. However, garnet crystals which do not deform viscously at 550 °C eventually accumulate stress at the level of yielding and deform plastically.

Finally, the fourth style (Style 4 in Fig. 5b) is characterized by frictional deformation inside of the whole model. During shearing of the model there is no rotation of the garnets. Plots of plastic strain and strain rate show flat-lying, parallel shear bands across the model. Although the whole model deforms plastically, there is still some component of viscous deformation in the matrix, which results in a negligible difference in the accumulated plastic strain and shear stress between matrix and garnet crystals. The only difference between these models and those with the garnet-amphibolite assemblage is the fact that the amphibolitic matrix is rheologically stronger than the quartzite, namely the frictional/viscous transition occurs at slightly higher depths or for faster strain rates (see also the comparative strength envelopes in Fig. S6).

To decipher the connection between the styles of deformation and normalized stress, we map the normalized stress in the garnet as a function of the pore fluid pressure ratio, λ, and the bulk shear strain rate, $\dot{\gamma}$, with isolines separating the different styles of deformation, which are given by the markers (Fig. 6). To underline the behavior of our models at very high pore fluid pressure ratios (typically >0.95 for subduction zones; Sibson, 2013; Angiboust et al., 2015), we separate our results into

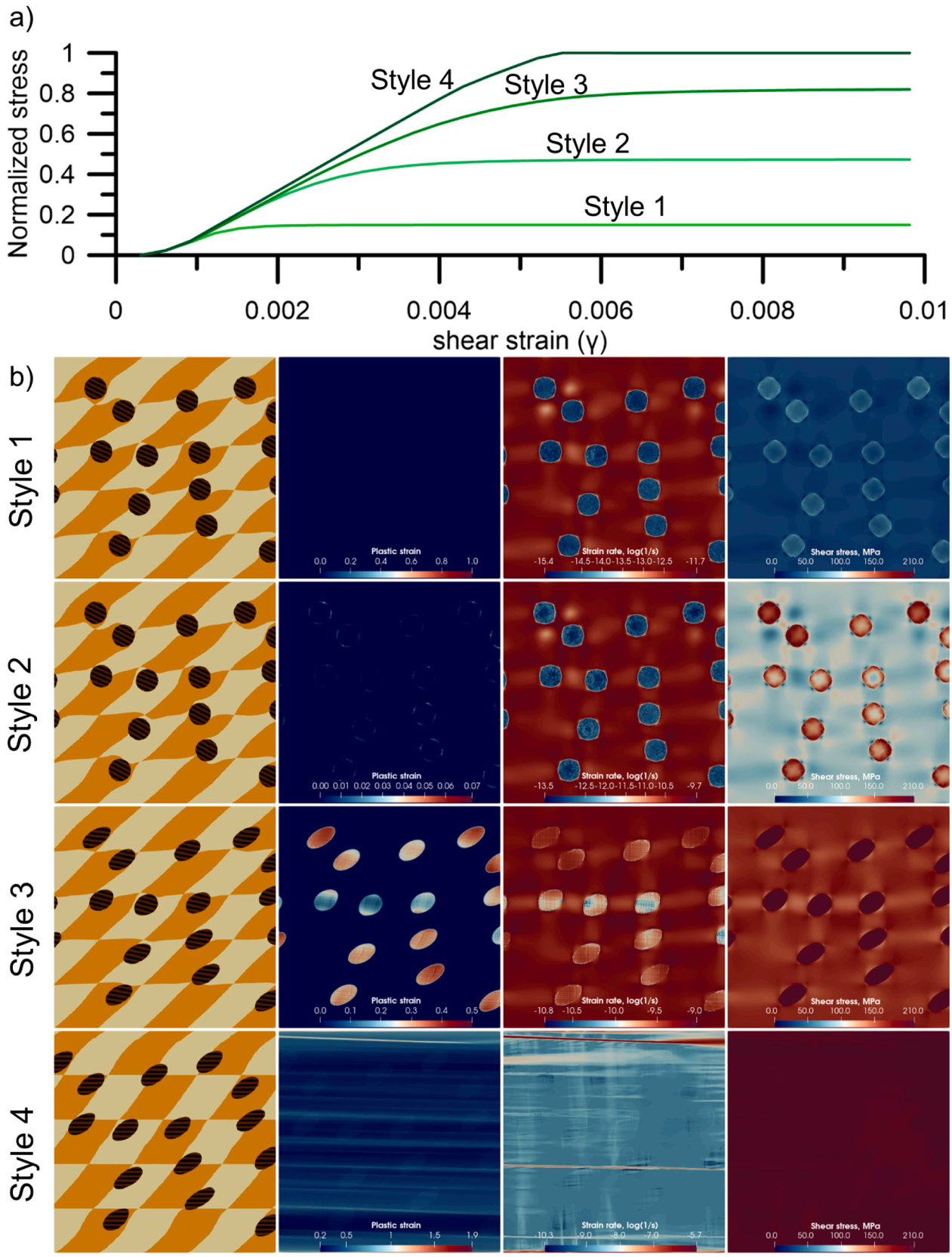

Fig. 5. Modelling - parameter exploration. a. Evolution of the normalized stress over shear strain. b. In columns: material distribution, accumulated plastic strain, strain rate, and shear stress at the final state of the models. Note that plastic strain in the second column refers to accumulated strain due to frictional deformation. In rows: Style 1 – no frictional deformation in the whole model ($\dot{\gamma} = 10^{-12}\frac{1}{s}$), Style 2 – frictional deformation only on the rims of the garnets ($\dot{\gamma} = 10^{-10}\frac{1}{s}$), Style 3 – frictional deformation only inside of garnets ($\dot{\gamma} = 10^{-9}\frac{1}{s}$), Style 4 – frictional deformation throughout the whole model ($\dot{\gamma} = 10^{-7.5}\frac{1}{s}$).

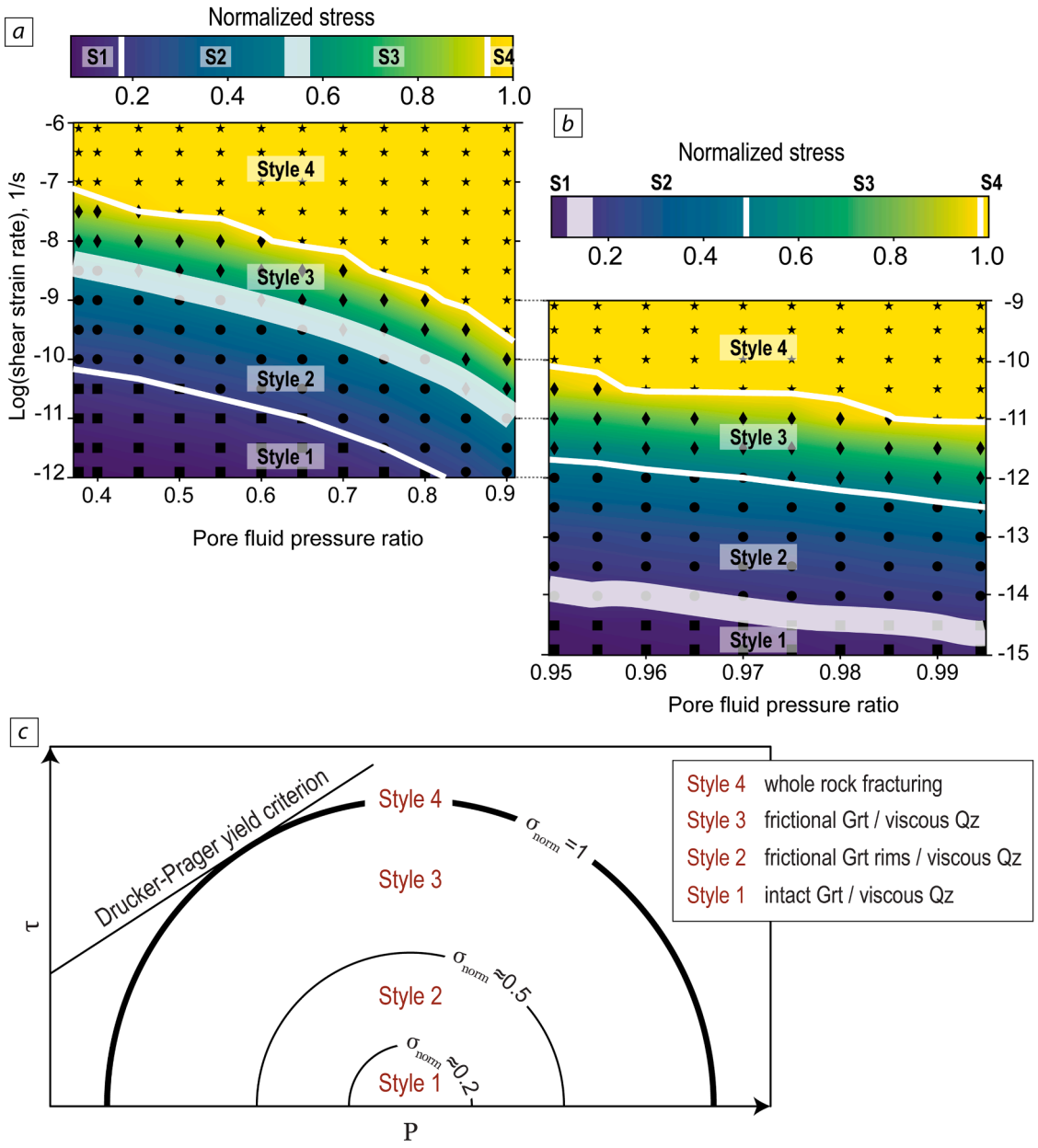

Fig. 6. Modelling – Normal stress and deformation style. a. Contour map of the normalized stresses of the quartzitic micaschist models with relatively high strain rates and low pore fluid pressure ratios. Markers denote the different deformation styles, while white lines mark the transition from one deformation style to another. b. Same as a, for lower strain rates and higher pore fluid pressure ratios. Note that even though we ran the model up to 10^{-4} 1/s, the results between 10^{-6} and 10^{-4} 1/s are not displayed here as they show similar features over this range. c. Modified Mohr diagram where the shear stress in the y-axis has been replaced by the normalized stress (Eq. (6)). P corresponds to the total pressure (Eq. (3)). The inclined straight line denotes the rock failure envelope ($\sigma_{norm} = 1$). The homocentric circles denote the maximum calculated σ_{norm} for the different deformation styles of our models. Grt stands for garnet, Qz for quartz.

two sub-figures: Fig. 6a on the left shows the normalized stresses for relatively low pore fluid pressure ratios (from hydrostatic conditions to $\lambda = 0.90$) and faster strain rates (10^{-12} to 10^{-6} 1/s); Fig. 6b on the right shows the normalized stresses for high pore fluid pressure ratios ($\lambda \geq 0.95$) and lower strain rates (10^{-15} to 10^{-9} 1/s). The equivalent plots for the garnet-amphibolite models are presented in Fig. S7a and b.

At low pore fluid pressure ratios (Fig. 6a) and low strain rates, all models deform viscously (Style 1 and to some extent Style 2 in Fig. 5b). As either strain rates or pore fluid pressures increase, shearing of the sample is accommodated by frictional failure in garnet, while the matrix remains viscous (Style 3). Finally, when strain rate is above 10^{-7} 1/s, pore fluid pressure does not play a role in the type of deformation; strain rate is high enough that both minerals deform frictionally (Fig. 6a and Style 4 in Fig. 5b). The white lines in Fig. 6 denote the aforementioned transitions between deformation styles and show a clear dependency on pore fluid pressure and strain rate. Notably, strain rates that promote frictional failure in the models (Style 3 and 4) can vary up to two orders of magnitude for the different pore pressures examined here.

When pore fluid pressure ratios are very elevated ($\lambda \geq 0.95$; Fig. 6b), deformation depends less on λ, as attested by the almost horizontal white lines, and more on strain rate. The lowest strain rates produce viscous deformation (Style 1 and 2), while for $\dot{\gamma} > 10^{-12.5}$ 1/s, frictional-viscous (Style 3) and frictional (Style 4) deformation prevails in the models. It is important to note that even though we prescribe a background strain rate, locally the strain rate may increase up to a few orders of magnitude inside the model (see right column of Fig. 5b).

Interestingly, models with the same style of deformation appear in the fixed range of normalized stress regardless of their λ and $\dot{\gamma}$: Style 1

appears in the range [0, ~0.2], Style 2 appears in the range [~0.2, ~0.5], Style 3 appears in the range [~0.5, ~0.99], and Style 4 appears only when σ_{norm} is 1. It should be noted, however, that there is some overlap in the σ_{norm} values between Style 1 and 2 (thick white line in high λ models), and Style 2 and 3 (thick white line in low λ models). The aforementioned overlap occurs due to our strict approach in style definition. For example, for a model to be classified as Style 2, it must have at least one element with non-zero plastic deformation on the rim of the garnet crystal but no elements with plastic deformation anywhere else inside of the observation area at the end of the simulation. However, models with different pore fluid pressures and shear strain rates but with equal peak stresses might reach peak stress at slightly different strains. This leads to different relative positions of garnet crystals at the moment when they reach peak stress, which consequently varies the stress field inside of the model and might cause yielding. Tables S2 and S3 provide all the values used for creating Fig. 6. Comparable ranges are also observed for the garnet-amphibolite models (Tables S4-S5, Fig. S7).

5. Discussion

5.1. Limitations of the numerical models

We have assumed a bi-mineralic composition (garnet and quartz or garnet and amphibolite) for the numerical models, even though exhumed rocks show a more complex composition with minor amounts of other phases such as white mica, amphibole, albite or epidote. However, the inclusion of more phases would increase the complexity of the model and would make interpretation of the results impossible. Moreover, garnet is the mineral in the assemblage which shows the more distinct microstructural characteristics of fracturing. We therefore focus our modelling investigations on this phase, even though a much higher ratio of strong phases (e.g., competent/brittle feldspar crystals) can in some cases influence the rheology of the modelled assemblage (Yamato et al., 2019; Beall et al., 2019; Ioannidi et al., 2021; Rogowitz et al., 2023).

Also, our stress estimates apply for temperature-depth conditions ($T > 500$ °C, depth>30–40 km) where dislocation creep and pressure solution creep (PSC) compete as prevalent deformation mechanism (Stöckhert, 2002; Fagereng and Den Hartog, 2017). In any case, PSC could not be modeled here due to the scarcity of available flow laws for high temperature conditions (see Smye and England, 2023 and references therein for a quantitative estimate of uncertainties associated with PSC laws). We therefore consider dislocation creep as the only viscous mechanism for both minerals at 1.3 GPa and 550 °C. Nonetheless, the evaluation of stresses in the matrix based only on (quartz or amphibolite) dislocation creep flow law should be considered as an upper bound (e.g., Wallace et al., 2012; Smye and England, 2023 and references therein). This is because (i) deformation via PSC is known to occur at lower stresses than those necessary for activating dislocation creep, and (ii) the white mica in the matrix foliation would likely accommodate part of the total plastic strain. In addition, there exists uncertainties in the dislocation creep parameters (A, n, Q) derived from laboratory experiments. Therefore, although the succession of the deformation styles would remain the same for different creep parameters, the absolute values of strain rates and stresses may vary to some extent. This is further corroborated by the similarity between the garnet-quartzite and the garnet-amphibolite models: the deformation styles, their relevant succession, as well as the comparable stress ranges associated with each deformation style are comparable. For the sake of clarity, in this manuscript, we consider low strain rates values $\leq 10^{-11}$ 1/s and high values $\geq 10^{-7}$ 1/s; values in between are then referred to as moderate (typically 10^{-8} 1/s).

We also add that due to the nature of our numerical approach (FEM is a continuum mechanics formulation), it is not possible for the material to fracture, creating new interfaces. Therefore, frictional deformation is approximated by flow instead of spatial discontinuity (fracturing). As a consequence, garnet crystals do not fracture but become elongated towards the shearing direction and consequently remain apparently bounded to the original crystal in these sheared domains. Note that a similar macroscopic pattern has been reported in cataclastically-deformed garnet crystals from the high-pressure Sesia zone in the Italian Alps (Trepmann and Stöckhert, 2002). Last, one challenge of our study is to bridge the gap between garnet-fracture scale (mm) and plate interface scales (tens of km). Our models and the structures formed therein are treated as scale-independent and self-similar, as commonly considered in similar studies (e.g. Fagereng, 2011; Grigull et al., 2012, Ioannidi et al., 2021). We therefore assume a fractal distribution of the structures that allows to some extent the extrapolation of our model results to subduction shear zone space scales.

5.2. Comparison with previous studies

Numerous mechanical studies have investigated the rheology of two-phase rock assemblages, experimentally (e.g., Ji et al., 2000; Jin et al., 2001; Rybacki et al., 2003), numerically (Kenkmann and Dresen, 1998; Beall et al., 2019a,b; Yamato et al., 2019; Ioannidi et al., 2021; 2022; Rogowitz et al., 2023), theoretically (e.g., Huet et al., 2014), or using natural samples (Handy et al., 1990; Grigull et al., 2012). Most garnet porphyroclasts studied previously were metamorphosed under eclogite facies conditions (Yamato et al., 2019; Rogowitz et al., 2023) and hence are embedded in an omphacite-bearing matrix, the rheology of which is much stronger than quartz as in our experiment. A stronger matrix (i.e. amphibolitic) enables the accumulation of stresses sufficient to produce deformation within the clast under a slightly lower strain rate than in the weak matrix (e.g., compare Style 3 deformation in Fig. 6a vs. Figs. S7a and 6b vs. Fig. S7b, or the yellow regions between Tables S2 and S4, and S3 and S5; see also Beall et al., 2019; Ioannidi et al., 2022). Yamato et al. (2019) found that locally increased stresses at the grain boundaries of garnet crystals can reach their yield strength and cause frictional failure; this deformation might be analogous to our Style 2 deformation. Moreover, varying volume fractions of garnet crystals would also result in varying the rheological behavior of the eclogite. This is also supported by Rogowitz et al. (2023) who studied omphacite-garnet assemblages (experimentally and numerically) and reported that larger fractions of garnet crystals resulted in higher strain localization in their samples. The high garnet-content models of both studies would correspond to the load-bearing framework of Handy (1990) where the strength of the aggregate depends primarily on that of the strong constituent phase. In our numerical study, however, the garnet content is relatively low (10 %), therefore a load-bearing framework is never achieved. Instead, our numerical rock assemblage shows characteristics of either a clast-in-matrix (Style 1 and 2) or a boudin-matrix rheology (Style 3), according to the classification by Handy (1990). Rogowitz et al. (2023) also reported the co-existence of both frictional and viscous (dislocation creep) features in the garnet crystals. In our models, we do not observe any viscous deformation of the garnet crystals, even in Style 1, where there is no frictional/plastic deformation either. The difference between our results and those of Rogowitz et al. (2023) mostly arise due to the lower PT conditions of our experiment compared to their models (1000 °C and 2.5 GPa, respectively) and perhaps to some extent due to the use of a different garnet flow law.

5.3. Garnet as a witness of ancient unstable slip events

While fractured, decapitated or truncated porphyroclasts are a common feature in strained metamorphic rocks, estimating the strain rates that led to these microstructures is a challenging task (e.g., Küster and Stöckhert, 1999; Johnson et al., 2021). Garnet fracturing as a record of co-seismic deformation has been proposed in pseudotachylyte-bearing mylonitic gneisses, i.e., in material that slipped at seismic strain rates during metamorphism in the granulite facies (e.g. Austrheim et al., 1996; Hawemann et al., 2019). Trepmann and

Stöckhert (2002) use the presence of fractured and offset garnet crystals as a marker of syn-seismic loading and subsequent post-seismic creep. However, it is clear that not all healed fractures in garnet should be interpreted in terms of unstable, fast-slip events. Fracturing of garnet has been reported in retrogressed metamorphic rocks undergoing exhumation-related deformation (e.g. Ji et al., 1997; Giuntoli et al., 2018). Other processes such as crystal indentation, crack-tip propagation and associated pressure-solution during ductile shearing can locally lead to sufficiently high stresses to reach the garnet brittle envelope (e.g., Prior, 1993; Rubatto et al., 2020). Numerical simulations by Yamato et al. (2019) have revealed that whole-rock shearing of an eclogite at moderate strain rates (for instance 10^{-8} 1/s) can generate garnet rupture without involving seismic slip rates. Unlike these previous experiments, we deal here with two phases which exhibit an extreme viscosity contrast (more than 5 orders of magnitude at 550 °C). Our numerical results indicate that when a quartz- or amphibolite-rich/garnet-poor matrix is affected by shearing, the only possibility for having garnet crystals to break without any rotation is to have the formation of localized, foliation-parallel bands in which both the matrix and the clasts behave in a brittle fashion (Style 4). This pattern may occur for strain rates covering a range from slow earthquakes to just before the onset of long-term creep (Oncken et al., 2022), depending on the pore fluid pressure ratio (Fig. 6).

Garnet fracturing in HP metasediments is rarely documented in exhumed suture zones and most garnet morphologies appear undisturbed in their major element zoning patterns. The pervasive fracturing of solitary garnet crystals in a quartzitic micaceous or mafic tuffaceous matrix as observed in Diego de Almagro Puerto Shear Zone samples thus points to anomalous conditions with respect to standard subduction slab-top environments (even though subduction margins are known to strongly differ from one context to the other). It also requires a large number of rock fracturing events as indicated by the highly shattered nature of garnet porphyroclasts (see Fig. 3) - even though the precise number of brittle events cannot be estimated. Nearly-lithostatic pore fluid pressure is expected for all deep SZ settings as demonstrated in numerous geophysical and geological studies (Peacock et al., 2011; Angiboust et al., 2015; Herviou et al., 2023). It is thus inferred from our numerical investigations that acceleration of strain rate from standard subduction zones conditions (10^{-12} 1/s) to localized, 'faster' slip conditions (from 10^{-11} or 10^{-10} 1/s for high λ values to higher than 10^{-4} 1/s for lower λ values) is required to trigger the deformation pattern depicted in Style 4, namely, the cataclasis of the rock volume (Fig. 7a). While the earlier 'slow' deforming conditions can easily be envisioned during interseismic creeping between two slip events, the latter 'faster' conditions might correspond in nature to accelerated slip rate, for instance during post-seismic relaxation or SSEs (Fig. 7).

From these observations, we can propose that the studied sample corresponds to a (cryptic) cataclasite which has been later foliated upon slip rate deceleration (and subsequent exhumation-related dynamic recrystallization; see also Sibson, 1980). Given the size of fractured fragments (several hundreds of microns in diameter; see Fig. S1, S5), it is clear that the fracturing of the studied sample has not occurred in a fault core itself (gouge) where hundred-times smaller fragments are expected (Johnson et al., 2021). So, what happened with the fault core? One possibility is that its extremely fine-grained nature has caused the total replacement of the matrix during exhumation-related re-equilibration.

Last, the thermal gradient at the time of brecciation was elevated (c.12 °C/km; Angiboust et al., 2018) and likely representative of a warm subduction regime similar to the one that can presently be observed in Nankai or Cascades interfaces (Peacock, 1996). Because such young subducted plates are characterized by a well-defined downdip limit of megathrust earthquakes at near 350 °C, well-above the upper plate Moho (Oleskevich et al., 1999), we speculate that the observed paleoseismicity does not directly reflect the propagation of a megathrust rupture down to c.45 km depth (i.e. at studied fracturing conditions). Instead, this depth corresponds in warm active margins to the region affected by slow earthquakes (e.g. Obara & Kato, 2016; Fig. 7b), inferred to occur on the interface itself (so, probably in a sediment-rich environment).

We conclude emphasizing that (i) the foliated cataclasite herein studied could record some of the transient creep events associated with slow slip event phenomena (in line with Oncken et al., 2022) and that (ii) cataclasis and brittle creep (in the sense of Brantut et al., 2013) should be viewed as a prevalent deformation mechanism operating in deep, fluid-rich, subduction fault systems (and not restricted to shallow crustal conditions as classically envisioned in rheological profiles).

6. Conclusions

We have presented 2D numerical models that shed light on fracturing and viscous deformation of a high-pressure, bi-mineralic block-in-matrix assemblage, composed of garnet within either a quarzitic or an amphibolitic matrix. Our results for both sets of models show that the style of deformation depends on the ratio of the stress in the matrix and its yield strength (namely the normalized stress), which is modulated by strain rate and pore fluid pressure ratio. Higher strain rate and higher pore fluid pressure ratio favor high stress in the model. For fixed pore fluid pressure conditions and for slow strain rates, minor clast rotation

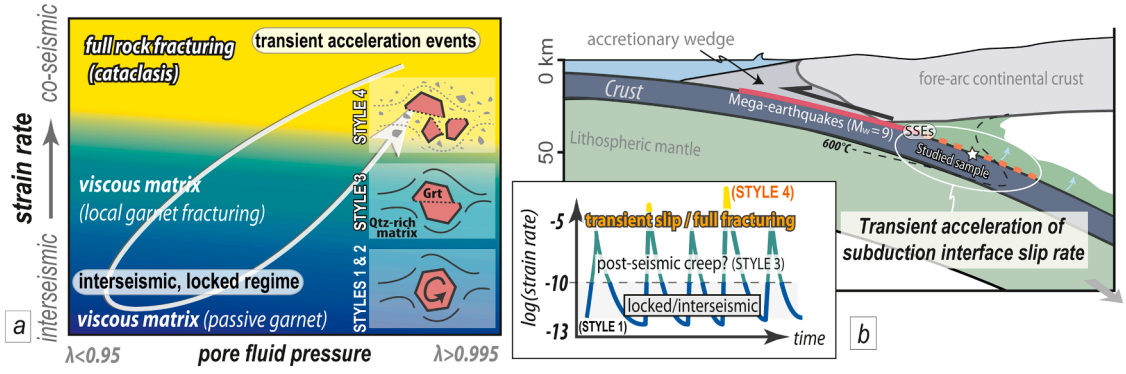

Fig. 7. Conceptual figure. a. Sketch depicting the influence of strain rate on the deformation style of garnet in our experiments. The conditions enabling the fracturing of garnet in a weak quartzitic matrix are met under relatively fast slip rates (possibly co-seismic) and extremely high pore fluid pressure conditions. The arrow depicts a possible mechanism for changing from one deformation style to another as a function of pore fluid pressure and strain rate fluctuations. Multiple brittle deformation cycles are required for explaining the garnet shattering as observed in the studied sample. b. Sketch of a subduction zone localizing the megathrust zone (red line), the slow slip events area (SSEs) and the location of the sample at the time of cataclasis (star). The base of the Lazaro unit (that hosts the transient deformation events herein studied) is involved in the anastomosing networks which constitute the volume forming the subduction interface (in the sense of Behr and Burgmann, 2021). The inset shows a conceptual series of 5 seismic cycles and the corresponding deformation modes at each stage of the cycle.

and distributed matrix deformation are observed. As strain rate increases, garnet becomes brittle, and instead of rotating, it develops internal shear bands which lead to its fracturing, while the matrix remains viscous. Finally, at the fastest strain rates, both matrix and garnet fracture, with distinct shear bands forming throughout the model. The latter pattern can explain the pervasively fractured garnet crystals found in a metasediment exhumed from the former Patagonian subduction interface region where 'lost' fast-slipping events (i.e. via conventional earthquakes or more likely, slow earthquakes) probably took place via cataclastic flow. Our study calls for a re-appraisal of cryptic microstructures in garnet-bearing metasediments that are likely to have hosted unstable slip events along ancient tectonic plate boundary settings.

CRediT authorship contribution statement

Samuel Angiboust: Funding acquisition, Investigation, Conceptualization, Data curation, Methodology, Project administration, Resources, Software, Validation, Writing – original draft, Writing – review & editing. **Paraskevi Io Ioannidi:** Conceptualization, Formal analysis, Investigation, Methodology, Resources, Software, Validation, Visualization, Writing – original draft, Writing – review & editing. **Iskander Muldashev:** Writing – review & editing, Conceptualization, Formal analysis, Investigation, Methodology, Resources, Software, Validation, Visualization, Writing – original draft.

Declaration of competing interest

The authors declare that they have no known competing financial interests or personal relationships that could have appeared to influence the work reported in this paper.

Data availability

Data will be made available on request.

Acknowledgments

O. Oncken, T. Hyppolito, M. Calderon and J. Muñoz-Montecinos are acknowledged for insightful discussions and assistance in the field. A. Smye and A. Rogowitz have provided useful and constructive comments for improving this work.

Supplementary materials

Supplementary material associated with this article can be found, in the online version, at doi:10.1016/j.epsl.2024.118794.

Appendix

– additional petrological data.
– additional numerical modelling information.

References

Angiboust, S., Menant, A., Gerya, T., Oncken, O., 2022. The rise and demise of deep accretionary wedges: a long-term field and numerical modeling perspective. Geosphere 18 (1), 69–103.
Angiboust, S., Cambeses, A., Hyppolito, T., Glodny, J., Monié, P., Calderón, M., Juliani, C., 2018. A 100-my-long window onto mass-flow processes in the Patagonian Mesozoic subduction zone (Diego de Almagro Island, Chile). GSA Bull. 130 (9–10), 1439–1456.
Angiboust, S., Kirsch, J., Oncken, O., Glodny, J., Monié, P., Rybacki, E., 2015. Probing the transition between seismically coupled and decoupled segments along an ancient subduction interface. Geochem. Geophys. Geosyst. 16 (6), 1905–1922.
Angiboust, S., Agard, P., Yamato, P., Raimbourg, H., 2012. Eclogite breccias in a subducted ophiolite: a record of intermediate-depth earthquakes? Geology 40 (8), 707–710.
Atkinson, B.K., 1984. Subcritical crack growth in geological materials. J. Geophys. Res.: Solid Earth 89 (B6), 4077–4114.
Austrheim, H., Andersen, T.B., 2004. Pseudotachylytes from Corsica: fossil earthquakes from a subduction complex. Terra nova 16 (4), 193–197.
Austrheim, H., Erambert, M., Boundy, T.M., 1996. Garnets recording deep crustal earthquakes. Earth Planet. Sci. Lett. 139 (1–2), 223–238.
Beall, A., Fagereng, Å., Ellis, S., 2019. Strength of strained two-phase mixtures: application to rapid creep and stress amplification in subduction zone mélange. Geophys. Res. Lett. 46 (1), 169–178.
Bebout, G.E., Penniston-Dorland, S.C., 2016. Fluid and mass transfer at subduction interfaces—The field metamorphic record. Lithos 240, 228–258.
Behr, W.M., Bürgmann, R., 2021. What's down there? The structures, materials and environment of deep-seated slow slip and tremor. Philosoph. Trans. R. Soc. A 379 (2193), 20200218.
Brantut, N., Heap, M.J., Meredith, P.G., Baud, P., 2013. Time-dependent cracking and brittle creep in crustal rocks: a review. J. Struct. Geol. 52, 17–43.
Condit, C.B., French, M.E., Hayles, J.A., Yeung, L.Y., Chin, E.J., Lee, C.T.A., 2022. Rheology of metasedimentary rocks at the base of the subduction seismogenic zone. Geochem. Geophys. Geosyst. 23 (2), e2021GC010194.
Connolly, J.A.D., 2005. Computation of phase equilibria by linear programming: a tool for geodynamic modeling and its application to subduction zone decarbonation. Earth Planet. Sci. Lett. 236 (1–2), 524–541.
Fagereng, Å., 2011. Fractal vein distributions within a fault-fracture mesh in an exhumed accretionary mélange, Chrystalls Beach Complex, New Zealand. J. Struct. Geol. 33 (5), 918–927. https://doi.org/10.1016/j.jsg.2011.02.009.
Fagereng, Å., Den Hartog, S.A., 2017. Subduction megathrust creep governed by pressure solution and frictional–viscous flow. Nat. Geosci. 10 (1), 51–57.
Freymueller, J.T., Woodard, H., Cohen, S.C., Cross, R., Elliott, J., Larsen, C.F., Hreinsdóttir, S., Ekström, G., 2008. Active deformation processes in Alaska, based on 15 years of GPS measurements. Active Tectonics Seismic Potential Alaska 179, 1–42.
Giuntoli, F., Lanari, P., Engi, M., 2018. Deeply subducted continental fragments: I. Fracturing, dissolution-precipitation and diffusion processes recorded by garnet textures of the central Sesia Zone (Western Italian Alps). Solid Earth 9, 167–189.
Gleason, G.C., Tullis, J., 1995. A flow law for dislocation creep of quartz aggregates determined with the molten salt cell. Tectonophysics 247 (1–4), 1–23.
Grigull, S., Krohe, A., Moos, C., Wassmann, S., Stöckhert, B., 2012. Order from chaos": a field-based estimate on bulk rheology of tectonic mélanges formed in subduction zones. Tectonophysics 568, 86–101.
Hacker, B.R., Christie, J.M., 1990. Brittle/ductile and plastic/cataclastic transitions in experimentally deformed and metamorphosed amphibolit. Geophys. Monogr. Ser. 56 (100), 127–147.
Hacker, B.R., Peacock, S.M., Abers, G.A., Holloway, S.D., 2003. Subduction factory 2. Are intermediate-depth earthquakes in subducting slabs linked to metamorphic dehydration reactions? J. Geophys. Res.: Solid Earth 108 (B1).
Handy, M.R., 1990. The solid-state flow of polymineralic rocks. J. Geophys. Res.: Solid Earth 95 (B6), 8647–8661.
Hawemann, F., Mancktelow, N., Wex, S., Pennacchioni, G., Camacho, A., 2019. Fracturing and crystal plastic behaviour of garnet under seismic stress in the dry lower continental crust (Musgrave Ranges, Central Australia). Solid Earth 10 (5), 1635–1649.
Hervé, F., Fanning, C.M., 2003. Early Cretaceous subduction of continental crust at the Diego de Almagro archipelago, southern Chile. Episodes J. Int. Geosci. 26 (4), 285–289.
Herviou, C., Agard, P., Verlaguet, A., Gyomlai, T., Bonnet, G., Mendes, K., Plunder, A., 2023. Fractal Distribution of Subduction-Related Crack-Seal Veins (Schistes Lustrés, W. Alps): Implications for Fluid Flow and Rupture Processes at the Downdip End of the Seismogenic Zone. J. Geophys. Res.: Solid Earth 128 (10), e2022JB026317.
Huet, B., Yamato, P., Grasemann, B., 2014. The Minimized Power Geometric model: an analytical mixing model for calculating polyphase rock viscosities consistent with experimental data. J. Geophys. Res.: Solid Earth 119 (4), 3897–3924.
Hyppolito, T., Angiboust, S., Juliani, C., Glodny, J., Garcia-Casco, A., Calderón, M., Chopin, C., 2016. Eclogite-, amphibolite-and blueschist-facies rocks from Diego de Almagro Island (Patagonia): episodic accretion and thermal evolution of the Chilean subduction interface during the Cretaceous. Lithos 264, 422–440.
Hyppolito, T., Cambeses, A., Angiboust, S., Raimondo, T., García-Casco, A., Juliani, C., 2019. Rehydration of eclogites and garnet-replacement processes during exhumation in the amphibolite facies. Geol. Soc. 478 (1), 217–239. London, Special Publications.
Incel, S., Hilairet, N., Labrousse, L., John, T., Deldicque, D., Ferrand, T., Wang, Y., Renner, J., Morales, L., Schubnel, A., 2017. Laboratory earthquakes triggered during eclogitization of lawsonite-bearing blueschist. Earth Planet. Sci. Lett. 459, 320–331.
Ioannidi, P.I., Le Pourhiet, L., Agard, P., Angiboust, S., Oncken, O., 2021. Effective rheology of a two-phase subduction shear zone: insights from numerical simple shear experiments and implications for subduction zone interfaces. Earth Planet. Sci. Lett. 566, 116913.
Ioannidi, P.I., Bogatz, K., Reber, J.E., 2022. The impact of matrix rheology on stress concentration in embedded brittle clasts. Geochem. Geophys. Geosyst. 23 (3), 1–19. https://doi.org/10.1029/2021gc010127.
Ji, S., Zhao, P., Saruwatari, K., 1997. Fracturing of garnet crystals in anisotropic metamorphic rocks during uplift. J. Struct. Geol. 19 (5), 603–620.
Ji, S., Martignole, J., 1994. Ductility of garnet as an indicator of extremely high temperature deformation. J. Struct. Geol. 16 (7), 985–996.
Jin, Z.M., Zhang, J., Green, H.W., Jin, S., 2001. Eclogite rheology: implications for subducted lithosphere. Geology 29 (8), 667–670.
John, T., Schenk, V., 2006. Interrelations between intermediate-depth earthquakes and fluid flow within subducting oceanic plates: constraints from eclogite facies pseudotachylytes. Geology 34 (7), 557–560.

Johnson, S.E., Song, W.J., Vel, S.S., Song, B.R., Gerbi, C.C., 2021. Energy partitioning, dynamic fragmentation, and off-fault damage in the earthquake source volume. J. Geophys. Res.: Solid Earth 126 (11), e2021JB022616.
Kenkmann, T., Dresen, G., 1998. Stress gradients around porphyroclasts: palaeopiezometric estimates and numerical modelling. J. Struct. Geol. 20 (2–3), 163–173.
Kirkpatrick, J.D., Rowe, C.D., 2013. Disappearing ink: how pseudotachylytes are lost from the rock record. J. Struct. Geol. 52, 183–198.
Küster, M., Stöckhert, B., 1999. High differential stress and sublithostatic pore fluid pressure in the ductile regime—Microstructural evidence for short-term post-seismic creep in the Sesia Zone, Western Alps. Tectonophysics 303 (1–4), 263–277.
Lamb, S., 2006. Shear stresses on megathrusts: implications for mountain building behind subduction zones. J. Geophys. Res. 111, B07401.
Lange, D., Tilmann, F., Barrientos, S.E., Contreras-Reyes, E., Methe, P., Moreno, M., Heit, B., Agurto, H., Bernard, P., Vilotte, J.P., Beck, S., 2012. Aftershock seismicity of the 27 February 2010 Mw 8.8 Maule earthquake rupture zone. Earth Planet. Sci. Lett. 317, 413–425.
Luo, H., Wang, K., 2021. Postseismic geodetic signature of cold forearc mantle in subduction zones. Nat. Geosci. 14 (2), 104–109.
Moreno, M., Haberland, C., Oncken, O., Rietbrock, A., Angiboust, S., Heidbach, O., 2014. Locking of the Chile subduction zone controlled by fluid pressure before the 2010 earthquake. Nat. Geosci. 7 (4), 292–296.
Muñoz-Montecinos, J., Angiboust, S., Garcia-Casco, A., 2021. Blueschist-facies paleo-earthquakes in a serpentinite channel (Zagros suture, Iran) enlighten seismogenesis in Mariana-type subduction margins. Earth Planet. Sci. Lett. 573, 117135.
Muñoz-Montecinos, J., Angiboust, S., Cambeses, A., García-Casco, A., 2020. Multiple veining in a paleo–accretionary wedge: the metamorphic rock record of prograde dehydration and transient high pore-fluid pressures along the subduction interface (Western Series, central Chile). Geosphere 16 (3), 765–786.
Obara, K., Kato, A., 2016. Connecting slow earthquakes to huge earthquakes. Science 353 (6296), 253–257.
Oleskevich, D.A., Hyndman, R.D., Wang, K., 1999. The updip and downdip limits to great subduction earthquakes: thermal and structural models of Cascadia, south Alaska, SW Japan, and Chile. J. Geophys. Res.: Solid Earth 104 (B7), 14965–14991.
Oncken, O., Angiboust, S., Dresen, G., 2022. Slow slip in subduction zones: reconciling deformation fabrics with instrumental observations and laboratory results. Geosphere 18 (1), 104–129.
Passchier, C.W., Trouw, R.A.J., Zwart, H.J., Vissers, R.L.M., 1992. Porphyroblast rotation: eppur si muove*? J. Metamorph. Geol. 10 (3), 283–294.
Peacock, S.M., Christensen, N.I., Bostock, M.G., Audet, P., 2011. High pore pressures and porosity at 35 km depth in the Cascadia subduction zone. Geology 39 (5), 471–474.
Peacock, S.M., 1996. Thermal and petrologic structure of subduction zones. Subduc.: Top Bottom 96, 119–133.
Popov, A.A., Sobolev, S.V., 2008. SLIM3D: a tool for three-dimensional thermomechanical modeling of lithospheric deformation with elasto-visco-plastic rheology. Phys. Earth Planetary Interiors 171, 55–75.
Prior, D.J., 1993. Sub-critical fracture and associated retrogression of garnet during mylonitic deformation. Contrib. Mineral. Petrol. 113 (4), 545–556.
Rogowitz, A., Thielmann, M., Kraus, K., Grasemann, B., Renner, J., 2023. The effect of the garnet content on deformation mechanisms and weakening of eclogite: insights from deformation experiments and numerical simulations. Geochem. Geophys. Geosyst. 24 (3), e2022GC010743.
Rubatto, D., Burger, M., Lanari, P., Hattendorf, B., Schwarz, G., Neff, C., Keresztes Schmidt, P., Hermann, J., Vho, A., Günther, D., 2020. Identification of growth mechanisms in metamorphic garnet by high-resolution trace element mapping with LA-ICP-TOFMS. Contrib. Mineral. Petrol. 175 (7), 61.
Rybacki, E., Paterson, M.S., Wirth, R., Dresen, G., 2003. Rheology of calcite–quartz aggregates deformed to large strain in torsion. J. Geophys. Res.: Solid Earth 108 (B2).
Shiina, T., Nakajima, J., Matsuzawa, T., 2013. Seismic evidence for high pore pressures in the oceanic crust: implications for fluid-related embrittlement. Geophys. Res. Lett. 40 (10), 2006–2010.
Sibson, R.H., 1980. Transient discontinuities in ductile shear zones. J. Struct. Geol. 2 (1–2), 165–171.
Sibson, R.H., 2013. Stress switching in subduction forearcs: implications for overpressure containment and strength cycling on megathrusts. Tectonophysics 600, 142–152.
Sippl, C., Schurr, B., Asch, G., Kummerow, J., 2018. Seismicity structure of the northern Chile forearc from >100,000 double-difference relocated hypocenters. J. Geophys. Res.: Solid Earth 123 (5), 4063–4087.
Smye, A.J., England, P.C., 2023. Metamorphism and deformation on subduction interfaces: 2. Petrological and tectonic implications. Geochem. Geophys. Geosyst. 24 (1), e2022GC010645.
Sobolev, S.V., Babeyko, A.Y., 2005. What drives orogeny in the Andes? Geology 33, 617–620.
Stöckhert, B., 2002. Stress and deformation in subduction zones: insight from the record of exhumed metamorphic rocks. In: Geol. Soc., 200. Special Publications, London, pp. 255–274.
Trepmann, C.A., Stöckhert, B., 2002. Cataclastic deformation of garnet: a record of synseismic loading and postseismic creep. J. Struct. Geol. 24 (11), 1845–1856.
Tulley, C.J., Fagereng, Å., Ujiie, K., 2020. Hydrous oceanic crust hosts megathrust creep at low shear stresses. Sci. Adv. 6 (22), eaba1529.
Vrijmoed, J.C., Podladchikov, Y.Y., 2015. Thermodynamic equilibrium at heterogeneous pressure. Contrib. Mineral. Petrol. 170, 1–27.
Wallace, L.M., Fagereng, Å., Ellis, S., 2012. Upper plate tectonic stress state may influence interseismic coupling on subduction megathrusts. Geology 40 (10), 895–898.
Wassmann, S., Stoeckhert, B., 2013a. Rheology of the plate interface—dissolution precipitation creep in high pressure metamorphic rocks. Tectonophysics 608, 1–29.
Wassmann, S., Stöckhert, B., 2013b. Low stress deformation of garnet by incongruent dissolution precipitation creep. J. Struct. Geol. 46, 200–219.
Whitney, D.L., Evans, B.W., 2010. Abbreviations for names of rock-forming minerals. Am. Mineral. 95 (1), 185–187.
Yamato, P., Duretz, T., Angiboust, S., 2019. Brittle/ductile deformation of eclogites: insights from numerical models. Geochem. Geophys. Geosyst. 20 (7), 3116–3133.